PERGAMON

Control Engineering Practice 10 (2002) 697–711

CONTROL ENGINEERING PRACTICE

www.elsevier.com/locate/conengprac

Control of a heavy-duty robotic excavator using time delay control with integral sliding surface

Sung-Uk Lee*, Pyung Hun Chang

Department of Mechanical Engineering, Korea Advanced Institute of Science and Technology, Science Town, 373-1 Koosung-dong, Yusung-ku, Taejon 305-701, South Korea

Received 22 March 2001; accepted 14 December 2001

Abstract

The control of a robotic excavator is difficult from the standpoint of the following problems: parameter variations in mechanical structures, various nonlinearities in hydraulic actuators and disturbance due to the contact with the ground. In addition, the more the size of robotic excavators increase, the more the length and mass of excavator's links; the more the parameters of a heavy-duty excavator vary. A time-delay control with switching action (TDCSA) using *an integral sliding surface* is proposed in this paper for the control of a *21-ton robotic excavator*. Through analysis and experiments, we show that using an integral sliding surface for the switching action of TDCSA is better than using a PD-type sliding surface. The proposed controller is applied to straight-line motions of a 21-ton robotic excavator with a speed level at which skillful operators work. Experiments, which were designed for surfaces with various inclinations and over broad ranges of joint motions, show that the proposed controller exhibits good performance.

Keywords: Time-delay control; Robust control; Switching action; Robotic excavator; Trajectory control

1. Introduction

A hydraulic excavator is a multi-functional construction machine. Workers in the construction industry use it for tasks such as excavating, dumping, finishing, lifting work, etc. However, operators who control hydraulic excavators must be trained for many years to do such work quickly and skillfully. A hydraulic excavator has three links: boom, arm and bucket; and the operator has two arms. Thus, it is not easy for beginners to execute elaborate work that manipulates three links at the same time. Moreover, because the operators have to run work in various dangerous and dirty environments, the number of skillful operators is ever decreasing. For that reason, studying the automation of hydraulic excavators is necessary for improving productivity, efficiency, and safety.

The automation of hydraulic excavators has been studied by several researchers (Singh, 1997). Among the several tasks to be automated, Bradley and Seward (1998) developed the Lancaster University computerized intelligent excavator (LUCIE) and used it to automate the digging work. Stentz, Bares, Singh, and Rowe (1998) developed a complete system for loading trucks fully autonomously on a 25-ton robotic excavator. Chang and Lee (2002) automated straight-line motions on a 13-ton robotic excavator under working speed conditions. Here, the straight-line motion represents the important task of scraping or flattening the ground and serves as a fundamental element used as a basis for developing more complicated tasks. As illustrated in Fig. 1, the end-effector of the manipulator needs to be controlled to track a linear path on the task surface. An operator should manipulate three links simultaneously to execute it. Though an operator is skillful, performing the straight-line motions for a long time results in the fatigue of an operator and decreases productivity.

The control of robotic excavator is difficult from the standpoint of the following problems: parameter variations in mechanical structures, various nonlinearities in hydraulic actuators, and disturbance due to the contact with the ground. In mechanical structures, the inertial

*Corresponding author. Tel.: +82-42-869-3266; fax: +82-42-869-5226.

E-mail address: s_sulee123@cais.kaist.ac.kr (S.-U. Lee).

0967-0661/02/$ - see front matter
PII: S0967-0661(02)00027-8

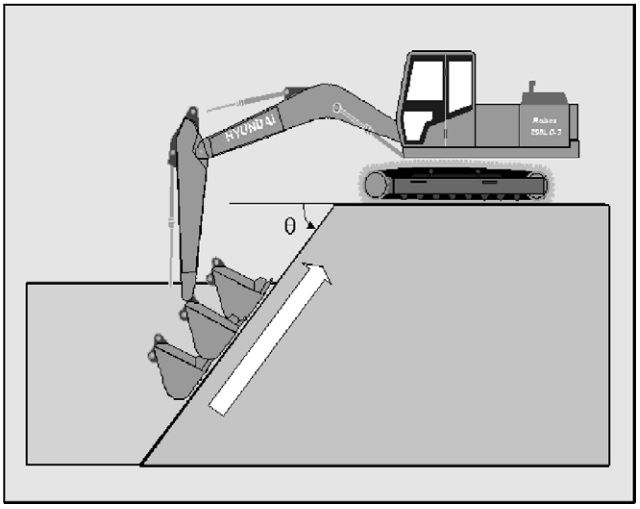

Fig. 1. Illustration of straight-line motion.

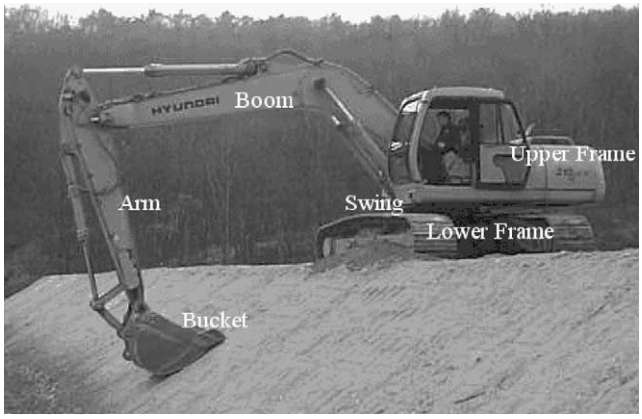

Fig. 2. Appearance of Robex210LC-3 excavator.

force and gravitational force varies largely with joint motions. Hydraulic actuators, massively coupled and complexly connected, have various nonlinear components. For such reasons, various difficulties exist in controlling a robotic excavator.

To solve these problems, several research works have been performed, which may be categorized as either simulation studies or experimental studies. In terms of simulation studies, for instance, Chiba and Takeda (1982) applied an optimal control scheme to the control of the manipulator of an excavator. Morita and Sakawa (1986) used PID control with feedforward control based on inverse dynamics. Medanic, Yuan, and Medanic (1997) proposed a polar controller-based variable structure control. Song and Koivo (1995) used a feedforward multiplayer neural network and a PID controller over a wide range of parameter variations. As for experimental studies, Bradley and Seward (1998) used a high-level controller that was based on rules obtained by observation of skilled operators, and a PID low-level motion controller that moved the end-effector in response to a demand from the high-level controller. Lee (1993) used P control together with a fuzzy control technique that used response error and its derivative on the phase plane. Sepehri, Lawrence, Sassani, and Frenette (1994) analyzed the phenomenon of coupling in the hydraulic actuator, and proposed a feedforward scheme that compensates coupling and load variation by using a simple valve model and measured pressure. Yokota, Sasao, and Ichiryu (1996) used disturbance observer and PI control, and applied it to a mini excavator. Chang and Lee (2002) used time-delay control (TDC) and compensators based on the dynamics of the excavator and applied it to straight-line motions of a 13-ton excavator with a bucket speed of 0.5 m/s, a speed level at which skillful operators work.

However, almost all the research works above tend to be limited to experiments on a mini excavator under relatively lower speed conditions. Among the experimental research works above, only that of Chang and Lee (2002), which was performed on the control of a heavy-duty 13-ton robotic excavator, was performed under working speed conditions. The more the size of excavators increase, the more the length and mass of excavator's links increase, and the more the parameters of a heavy-duty excavator vary. Therefore, the control of a heavy-duty excavator becomes more difficult than the control of a mini excavator. The control of a heavy-duty excavator (a 21-ton robotic excavator (Fig. 2) used in this paper) requires a robust controller.

In this paper, we apply time-delay control with switching action (TDCSA) using an *integral sliding surface* (ISS) to the control of a 21-ton robotic excavator and validate the proposed control algorithm through experiments on a straight-line motion tracking control. In addition, we show the advantage of the TDCSA using an ISS. TDCSA, which was proposed by Chang and Park (1998), consists of a TDC and a switching action. The switching action based on sliding mode control (SMC) compensates for the error of the time-delay estimation (TDE) and makes the TDC more robust. Chang and Park (1998) used a PD-type sliding surface (PDSS) for the switching action and applied the TDCSA using a PDSS to a pneumatic system for compensating the stick-slip, but we use an ISS for the switching action to improve the control performance in this paper (Slotine & Li, 1991; Utkin & Shi, 1996). As a similar controller, a new integral variable structure regulation controller, designed using an integral sliding surface and disturbance observer, was proposed by Lee and Youn (1999). Lee and Youn, however, have demonstrated the usefulness of their proposed algorithm by simulations about regulation controls of a two-link manipulator. In contrast, we will perform experiments on the control of a robotic excavator.

The rest of this paper is organized as follows. Section 2 will briefly analyze the characteristics of the robotic excavator system, Section 3 presents the design of controller. In Section 4, the effectiveness of the proposed controller will be verified through experiments on a 21-ton robotic excavator. Finally, conclusions will be drawn in Section 5.

2. Overview of robotic excavator system

This section describes briefly the characteristics of the robotic excavator. More details about the model of a robotic excavator can be found in Chang and Lee (2002). In this paper, the swing motor together with the traveling motor is not considered for straight-line motion; only the boom, arm and bucket are considered. The mathematical model that is needed for designing a controller is described in Appendix A. Since a robotic excavator consists of a manipulator and actuators, the characteristic of these two parts will be described briefly.

2.1. Manipulator

In the dynamic equation (Eq. (A.1)), the inertial forces and gravitational forces as well as the centrifugal and Coriolis forces vary nonlinearly with the change of angles of the links, and have coupling elements between links. Among these terms, the centrifugal and Coriolis forces have a smaller effect on the control performance, since the velocity of each link is not that great. In comparison, the inertial forces and gravitational forces vary largely, since the total weight of boom, arm and bucket used in this research is 2.67 ton and the range of joint angles are broad. The size and variation in each of the inertial and the gravitational forces in a straight-line motion with incline of 0° are shown in Fig. 3. We can observe that the inertial forces and gravitational forces vary largely.

2.2. Hydraulic actuators

The hydraulic actuator of the robotic excavator used in this paper has at least three kinds of nonlinearities as follows: valve characteristics, dead zone and time lag.

2.2.1. Valve characteristics

Hydraulic valves are devices that transfer the flow from the pump to cylinder. From the general valve flow equation ($Q = c_d A\sqrt{\Delta P}$), the flow that is transferred from the pump to cylinder is determined by flow coefficient, the area of the valve and pressure difference. The area of a spool valve has a nonlinear shape as shown in Fig. 4. Therefore, valves have nonlinear characteristics according to the nonlinear area of the valve and $\sqrt{\Delta P}$.

2.2.2. Dead zone

The geometry of the spool valve used in a Robex210LC-3 excavator is an overlapped shape as shown in Fig. 4 and causes the dead zone nonlinearity. The overlapped region is designed for the convenience of an operator. Therefore, when the spool is displaced in the overlapped region, the valve becomes closed: this causes

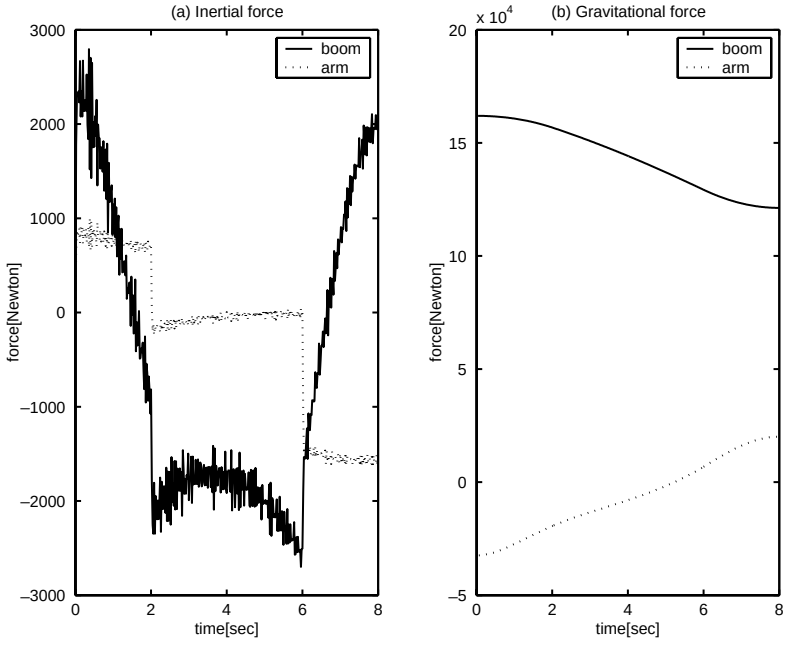

Fig. 3. Inertial forces and gravitational forces of boom and arm.

the dead zone nonlinearity. The overlapped region is about 30 percent of the whole spool displacement.

2.2.3. Time lag

A phenomenon similar to a dead zone occurs because of the time taken for the pump output pressure to reach the pressure level that is sufficient to move the link. Note that this phenomenon is somewhat different from the pure time delay often found in transmission lines. Fig. 5 illustrates this phenomenon with the experimental results. In the presence of maximum control input, the boom does not move until the time is 0.13 s, when the pump pressure begins to exceed the pressure of the boom cylinder plus the offset pressure, as shown in Fig. 5. This phenomenon occurs only when the boom link begins to move and it does not exist any more once the pump output pressure reaches the pressure level sufficient to move the link. Moreover, this phenomenon can be compensated by the compensator which will be proposed in Section 3.2.

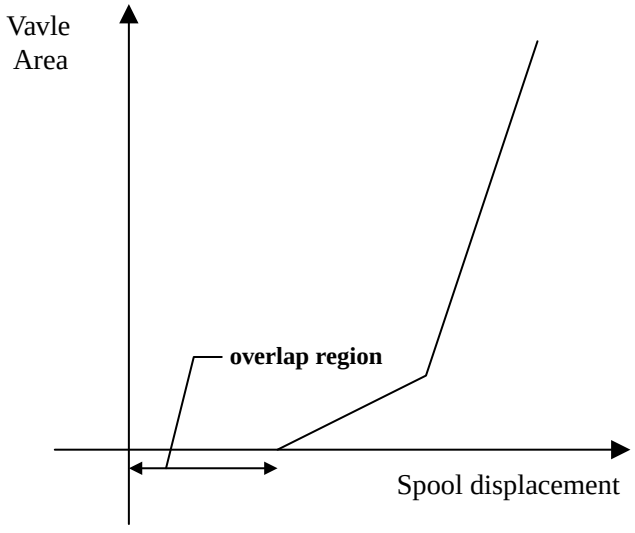

Fig. 4. Rough shapes for areas of spool valve.

3. Controller design

A robotic excavator has the following nonlinearities: variations in the inertial and gravitational forces in the manipulator; and nonlinear valve characteristics, dead zone and time lag in the hydraulic actuator. To overcome these aforementioned nonlinearities, Chang and Lee (2002) suggested the TDC and compensators and used these to control a 13-ton robotic excavator, but we need a more robust controller to control a 21-ton robotic excavator effectively. The greatest difference between the 21-ton robotic excavator used in this paper and the 13-ton robotic excavator used in Chang and Lee (2002) exists in the length and mass of excavator's links. The links of the former are one and half times the length and weight of those of the latter. Therefore, the parameter variations of a 21-ton excavator are more serious than those of a 13-ton excavator. A more robust controller than TDC is required to control the straight-line motion of a 21-ton robotic excavator.

For controlling a 21-ton robotic excavator, we have considered TDCSA, which is more robust than TDC.

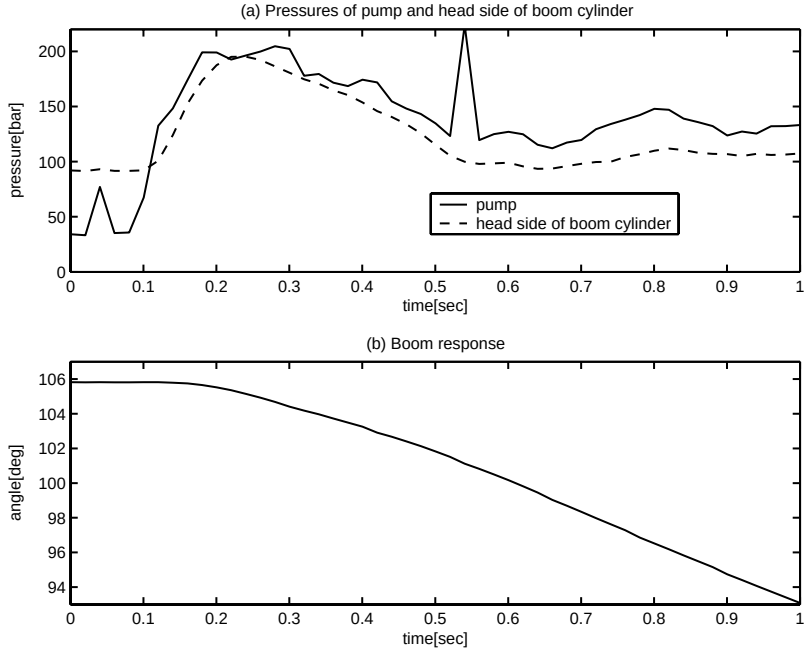

Fig. 5. Illustration of the nonlinearity due to time lag.

Then, instead of a PDSS used by Chang and Park (1998), we use an ISS in this paper for improving the control performance (Slotine & Li, 1991; Utkin & Shi, 1996).

Among the aforementioned nonlinearities, however, the dead zone and the time lag cause the large tracking errors. Hence, proper compensation is demanded. For that reason, we design the two controllers: first the TDCSA using an ISS as the *baseline control* and second, compensators to overcome the dead zone and the time lag.

3.1. Design of the TDCSA

3.1.1. TDCSA using an ISS

In order to apply the controller to a robotic excavator, Eq. (A.5) is rearranged into the following:

$$\bar{\mathbf{M}}\ddot{\mathbf{l}}(t) + \bar{\mathbf{H}}(t) = \mathbf{u}(t). \tag{1}$$

Note that $\bar{\mathbf{M}}$ is a constant matrix representing the known angle of $\mathbf{M}_K$, whereas $\bar{\mathbf{H}}(t)$ consists of terms representing uncertainties and time-varying factors, which are expressed as

$$\bar{\mathbf{H}}(t) = \mathbf{H}(t) + (\mathbf{M}_K(t) - \bar{\mathbf{M}})\ddot{\mathbf{l}}(t). \tag{2}$$

Now we define the desired dynamics of the closed-loop system with the following error dynamic:

$$\ddot{\mathbf{e}}(t) + \mathbf{K}_v\dot{\mathbf{e}}(t) + \mathbf{K}_p\mathbf{e}(t) = \mathbf{0}, \tag{3}$$

where $\mathbf{e}(t) = \mathbf{l}_d(t) - \mathbf{l}(t)$ denotes the position error vector with $\mathbf{l}_d(t)$ denoting the vector of desired piston displacements, $\mathbf{K}_v$ the derivative gain matrix, and $\mathbf{K}_p$ the proportional gain matrix. The TDC law that meets the requirement is obtained as

$$\mathbf{u}_{\mathrm{tdc}}(t) = \bar{\mathbf{M}}[\ddot{\mathbf{l}}_d(t) + \mathbf{K}_v\dot{\mathbf{e}}(t) + \mathbf{K}_p\mathbf{e}(t)] + \hat{\mathbf{H}}(t), \tag{4}$$

where $\hat{\mathbf{H}}(t)$ denotes an estimate of $\bar{\mathbf{H}}(t)$.

The estimated $\hat{\mathbf{H}}(t)$ can be obtained by using both Eq. (1) and the fact that $\bar{\mathbf{H}}(t)$ is usually a continuous function. More specifically, when L is small enough, then

$$\hat{\mathbf{H}}(t) \approx \bar{\mathbf{H}}(t-L) = \mathbf{u}(t-L) - \bar{\mathbf{M}}\ddot{\mathbf{l}}(t-L). \tag{5}$$

Combining Eq. (5) with Eq. (4), the TDC law is obtained as follows:

$$\mathbf{u}_{\mathrm{tdc}}(t) = \bar{\mathbf{M}}[\ddot{\mathbf{l}}_d(t) + \mathbf{K}_v\dot{\mathbf{e}}(t) + \mathbf{K}_p\mathbf{e}(t)] + \mathbf{u}_{\mathrm{tdc}}(t-L) - \bar{\mathbf{M}}\ddot{\mathbf{l}}(t-L). \tag{6}$$

More details about the stability condition and the design of TDC can be found in Youcef-Toumi and Ito (1990) and Hsia and Gao (1990).

L should be sufficiently small for TDC to meet the desired error dynamics of Eq. (3). The valve used for L, however, is set to be that of the sampling time, when TDC is implemented in a real-time controller. The variation of system nonlinearities and disturbances, occurred during the time delay (L), caused TDE error as follows:

$$\bar{\mathbf{H}}(t) - \hat{\mathbf{H}}(t) = \bar{\mathbf{H}}(t) - \bar{\mathbf{H}}(t-L) = \Delta\mathbf{H}(t). \tag{7}$$

More specifically, the friction dynamics cause large TDE error. Because of the TDE error, TDC does not have the desired error dynamics of Eq. (3), but the following error dynamics:

$$\ddot{\mathbf{e}}(t) + \mathbf{K}_v\dot{\mathbf{e}}(t) + \mathbf{K}_p\mathbf{e}(t) = \bar{\mathbf{M}}^{-1}\Delta\mathbf{H}(t), \tag{8}$$

where the right term ($\bar{\mathbf{M}}^{-1}\Delta\mathbf{H}(t)$) denotes the effect of the TDE error.

The TDCSA is proposed by adding the switching action based on the sliding mode control to TDC, as follows:

$$\mathbf{u}_{\mathrm{tdcsa}}(t) = \bar{\mathbf{M}}[\ddot{\mathbf{l}}_d(t) + \mathbf{K}_v\dot{\mathbf{e}}(t) + \mathbf{K}_p\mathbf{e}(t)] + \mathbf{u}_{\mathrm{tdcsa}}(t-L) - \bar{\mathbf{M}}\ddot{\mathbf{l}}(t-L) + \mathbf{K}_w\,\mathrm{sgn}(\mathbf{s}), \tag{9}$$

where $\mathbf{s}$ represents the sliding surface and $\mathbf{K}_w$ is a switching gain matrix. The TDCSA has the following error dynamic:

$$\ddot{\mathbf{e}}(t) + \mathbf{K}_v\dot{\mathbf{e}}(t) + \mathbf{K}_p\mathbf{e}(t) = \bar{\mathbf{M}}^{-1}\Delta\mathbf{H}(t) - \bar{\mathbf{M}}^{-1}\mathbf{K}_w\,\mathrm{sgn}(\mathbf{s}). \tag{10}$$

In Eq. (10), we see that the switching action can reduce the TDE error.

In order to match the desired error dynamics (Eq. (4)) with the sliding surface ($\mathbf{s}$), we use the integral sliding surface as follows:

$$\mathbf{s}(t) = \dot{\mathbf{e}}(t) + \mathbf{K}_v\mathbf{e}(t) + \mathbf{K}_p\int_0^t \mathbf{e}(\tau)\,\mathrm{d}\tau - \dot{\mathbf{e}}(0) - \mathbf{K}_v\mathbf{e}(0), \tag{11}$$

where the sliding surface ($\mathbf{s}$) has the initial value of zero and its derivative is equal to desired error dynamics (Eq. (3)). The necessity and advantage of using an integral sliding surface will be shown in Section 3.1.4.

3.1.2. Stability analysis of TDCSA using an integral sliding surface

For the stability analysis of the overall system, we use the second method of Lyapunov. If the Lyapunov function is selected as $\mathbf{V} = \frac{1}{2}\mathbf{s}^{\mathrm{T}}\mathbf{s}$, its time derivative is as follows:

$$\begin{aligned}
\dot{\mathbf{V}} &= \mathbf{s}^{\mathrm{T}}\dot{\mathbf{s}} = \mathbf{s}^{\mathrm{T}}[\ddot{\mathbf{e}} + \mathbf{K}_v\dot{\mathbf{e}} + \mathbf{K}_p\mathbf{e}] \\
&= \mathbf{s}^{\mathrm{T}}[\ddot{\mathbf{l}}_d - \bar{\mathbf{M}}^{-1}\mathbf{u} + \bar{\mathbf{M}}^{-1}\bar{\mathbf{H}} + \mathbf{K}_v\dot{\mathbf{e}} + \mathbf{K}_p\mathbf{e}] \\
&= \mathbf{s}^{\mathrm{T}}\{\ddot{\mathbf{l}}_d - \bar{\mathbf{M}}^{-1}[\bar{\mathbf{M}}(\ddot{\mathbf{l}}_d + \mathbf{K}_v\dot{\mathbf{e}} + \mathbf{K}_p\mathbf{e}) + \hat{\mathbf{H}} + \mathbf{K}_w\mathrm{sgn}(\mathbf{s})] \\
&\quad + \bar{\mathbf{M}}^{-1}\bar{\mathbf{H}} + \mathbf{K}_v\dot{\mathbf{e}} + \mathbf{K}_p\mathbf{e}\} \\
&= \mathbf{s}^{\mathrm{T}}[-\bar{\mathbf{M}}^{-1}\hat{\mathbf{H}} + \bar{\mathbf{M}}^{-1}\bar{\mathbf{H}} - \bar{\mathbf{M}}^{-1}\mathbf{K}_w\,\mathrm{sgn}(\mathbf{s})] \\
&= \mathbf{s}^{\mathrm{T}}[\bar{\mathbf{M}}^{-1}\Delta\mathbf{H} - \bar{\mathbf{M}}^{-1}\mathbf{K}_w\,\mathrm{sgn}(\mathbf{s})].
\end{aligned} \tag{12}$$

Therefore, the following condition is needed so that the time derivative of the Lyapunov function should be negative definite:

$$(K_w)_{ii} > |(\Delta H)_i| \quad \text{for } i = 1, \ldots, 3. \tag{13}$$

In other words, the magnitude of the switching gain ($\mathbf{K}_w$) must be larger than that of the term due to the TD estimation error.

3.1.3. Saturation function

TDCSA uses a switching action for compensating the TDE error, but the switching action in TDCSA causes a chattering problem. Therefore, we use a saturation function to reduce the chattering problem (Slotine & Li, 1991). A saturation function can be used as follows:

$$\mathrm{sat}(\mathbf{s}(t),\phi)=\begin{cases}\left(\frac{\mathbf{s}(t)}{\phi}\right) & \text{if } |\mathbf{s}(t)|<\phi,\\ \mathrm{sgn}(\mathbf{s}(t)) & \text{otherwise,}\end{cases}\tag{14}$$

where ϕ is the boundary layer of saturation function. As a result, TDCSA with saturation function is obtained as follows:

$$\mathbf{u}_{\mathrm{tdcsa}}(t)=\bar{\mathbf{M}}[\ddot{\mathbf{l}}_d(t)+\mathbf{K}_v\dot{\mathbf{e}}(t)+\mathbf{K}_p\mathbf{e}(t))+\mathbf{u}_{\mathrm{tdcsa}}(t-L)-\bar{\mathbf{M}}\ddot{\mathbf{l}}(t-L)+\mathbf{K}_w\,\mathrm{sat}(\mathbf{s},\phi).\tag{15}$$

By using sat(·) in the place of sgn(·), we can expect a reduction of the chattering in the control input and the state vector. If a large boundary layer is selected, the chattering will be reduced, but the tracking error will be increased. So, the proper selection of the boundary layer is needed.

3.1.4. The necessity and advantage of an ISS

In this section, we will study the necessity and advantage of the TDCSA using an ISS in comparison with the TDCSA using a PDSS.

3.1.4.1. The necessity of an integral sliding surface. TDCSA consists of TDC and switching action of SMC. TDC makes, on the one hand, the plant follow the desired error dynamics. On the other hand, the sliding surface for the switching action should be obtained from the desired error dynamics. Therefore, it becomes necessary to match the desired error dynamics of TDC and the derivative of the sliding surface—the equal error dynamics of SMC. More specifically, the ISS is given as $\mathbf{s}_{\mathrm{int}}=\dot{\mathbf{e}}(t)+\mathbf{K}_v\mathbf{e}(t)+\mathbf{K}_p\int\mathbf{e}(\tau)\,\mathrm{d}\tau-\dot{\mathbf{e}}(0)-\mathbf{K}_v(0)$. Its derivative becomes $\ddot{\mathbf{e}}(t)+\mathbf{K}_v\dot{\mathbf{e}}(t)+\mathbf{K}_p\mathbf{e}(t)=0$, which is equal to the desired error dynamics of TDC given in Eq. (3). In comparison, the PDSS is given as $\mathbf{s}_{pd}=\dot{\mathbf{e}}(t)+\lambda\mathbf{e}(t)$; the derivative of which is not equal to Eq. (3).

3.1.4.2. The advantage of an integral sliding surface. For the sliding surface inside the boundary layer (ϕ), the switching action of TDCSA using a PDSS and TDCSA using an ISS is obtained as Eqs. (16) and (17)

$$K_{w_i}\,\mathrm{sat}(s_{pd_i},\phi_i)=\frac{K_{w_i}}{\phi_i}(\dot{e}_i(t)+\lambda_i e_i(t)),\quad \text{for } |s_{pd_i}|\leqslant\phi_i,\tag{16}$$

$$K_{w_i}\mathrm{sat}(s_{int_i},\phi_i)=\frac{K_{w_i}}{\phi_i}\left(\dot{e}_i(t)+K_{v_i}e_i(t)+K_{p_i}\int e_i(\tau)\,\mathrm{d}\tau\right),\quad \text{for } |s_{int_i}|\leqslant\phi_i.\tag{17}$$

Combining Eqs. (16) and (17) each with Eq. (15), we can rearrange Eq. (15) into Eqs. (18) and (19), respectively:

$$\begin{aligned}u_{pd_i}(t)&=\bar{M}_i[\ddot{l}_{d_i}(t)+K_{v_i}\dot{e}_i(t)+K_{p_i}e_i(t)]+u_{pd_i}(t-L)\\&\quad-\bar{M}_i\ddot{l}_i(t-L)+\frac{K_{w_i}}{\phi_i}(\dot{e}_i(t)+\lambda_i e_i(t))\\&=\bar{M}_i\left[\ddot{l}_{d_i}(t)+\left(K_{v_i}+\bar{M}_i^{-1}\frac{K_{w_i}}{\phi_i}\right)\dot{e}_i(t)\right.\\&\quad\left.+\left(K_{p_i}+\bar{M}_i^{-1}\frac{K_{w_i}\lambda_i}{\phi_i}\right)e_i(t)\right]\\&\quad+u_{pd_i}(t-L)-\bar{M}_i\ddot{l}_i(t-L),\end{aligned}\tag{18}$$

$$\begin{aligned}u_{int_i}(t)&=\bar{M}_i[\ddot{l}_{d_i}(t)+K_{v_i}\dot{e}_i(t)+K_{p_i}e_i(t)]+u_{int_i}(t-L)\\&\quad-\bar{M}_i\ddot{l}_i(t-L)+\frac{K_{w_i}}{\phi_i}\left[\dot{e}_i(t)+K_{v_i}e_i(t)\right.\\&\quad\left.+K_{p_i}\int e_i(\tau)\,\mathrm{d}\tau\right]\\&=\bar{M}_i\left[\ddot{l}_{d_i}(t)+\left(K_{v_i}+\bar{M}_i^{-1}\frac{K_{w_i}}{\phi_i}\right)\dot{e}_i(t)\right.\\&\quad+\left(K_{p_i}+\bar{M}_i^{-1}\frac{K_{w_i}K_{v_i}}{\phi_i}\right)e_i(t)\\&\quad\left.+\bar{M}_i^{-1}\frac{K_{w_i}K_{p_i}}{\phi_i}\int e_i(\tau)\,\mathrm{d}\tau\right]+u_{int_i}(t-L)\\&\quad-\bar{M}_i\ddot{l}_i(t-L)\end{aligned}\tag{19}$$

From Eqs. (18) and (19), each closed-loop error dynamic is as follows:

$$\ddot{e}_i(t)+\left(K_{v_i}+\bar{M}_i^{-1}\frac{K_{w_i}}{\phi_i}\right)\dot{e}_i(t)+\left(K_{p_i}+\bar{M}_i^{-1}\frac{K_{w_i}\lambda_i}{\phi_i}\right)e_i(t)=\bar{M}_i^{-1}\Delta H_i(t),\tag{20}$$

$$\ddot{e}_i(t)+\left(K_{v_i}+\bar{M}_i^{-1}\frac{K_{w_i}}{\phi_i}\right)\dot{e}_i(t)+\left(K_{p_i}+\bar{M}_i^{-1}\frac{K_{w_i}K_{v_i}}{\phi_i}\right)\times e_i(t)+\bar{M}_i^{-1}\frac{K_{w_i}K_{p_i}}{\phi_i}\int e_i(\tau)\,\mathrm{d}\tau=\bar{M}_i^{-1}\Delta H_i(t).\tag{21}$$

Eq. (20) is the closed-loop error dynamic of TDCSA using a PDSS and Eq. (21) is that of TDCSA using an ISS. In Eqs. (20) and (21), the closed-loop error dynamic of TDCSA using a PDSS is similar to that of TDC, but differs in gain terms; however, the closed-loop error dynamic of TDCSA using an ISS has different integral term, which is caused by an ISS.

For the case where TDE error is constant ($\Delta H_i(t) =$ const.), $e_i(t)$ of Eq. (20) does not converge to 0. Thus, in the presence of any TDE error, a nonzero tracking error is unavoidable. As $t \to \infty$, $\ddot{e}_i(t) = \dot{e}_i(t) = 0$, and since $K_{w_i} > |\Delta H_i|$, the minimum tracking guarantee is

$$|e_{ss_i}| < \frac{\bar{M}_i^{-1}\,\Delta H_i(t)}{K_{p_i} + \bar{M}_i^{-1}(K_{w_i}\lambda_i/\phi_i)}. \tag{22}$$

For a constant right-hand side of Eq. (21), however, the steady-state solution of Eq. (21) is $e_i(t) \to 0$ and $\int_0^t e_i(\tau)\,d\tau \to 0$. Therefore, TDCSA using an ISS can drive the tracking errors resulting from bias in uncertainties (such as constant and slowly varying parametric errors) to zero.

From Eqs. (20) and (21), the relationship in the Laplace domain between the TDE error and position error ($e(t)$) is as follows:

$$\frac{E_i(p)}{\Delta H_i(p)} = \frac{\bar{M}_i^{-1}}{p^2 + (K_{v_i} + \bar{M}_i^{-1}(K_{w_i}/\phi_i))p + (K_{p_i} + \bar{M}_i^{-1}(K_{w_i}\lambda_i/\phi_i))}, \tag{23}$$

$$\begin{aligned}\frac{E_i(p)}{\Delta H_i(p)} &= \frac{\bar{M}_i^{-1}p}{p^3 + (K_{v_i} + \bar{M}_i^{-1}(K_{w_i}/\phi_i))p^2 + (K_{p_i} + \bar{M}_i^{-1}(K_{w_i}K_{v_i}/\phi_i))p + \bar{M}_i^{-1}(K_{w_i}K_{p_i}/\phi_i)} \\ &= \frac{\bar{M}_i^{-1}p}{(p + \bar{M}_i^{-1}(K_{w_i}/\phi_i))(p^2 + K_{v_i}p + K_{p_i})},\end{aligned} \tag{24}$$

where p is the Laplace operator. Eq. (23) is that of the TDCSA using a PDSS and Eq. (24) is that of the TDCSA using an ISS. The bode plot of Eqs. (23) and (24) is shown in Fig. 6. The TDCSA using an ISS has the same high-frequency behavior as the TDCSA using a PDSS and TDC. In the low-frequency range, however, TDCSA using an ISS has a lower gain than the other controller. Thus, the TDCSA using an ISS reduces effectively the position error, which is caused by TDE error in the low-frequency range, and then the TDCSA using an ISS is more robust than the other controller against the disturbances and variation of parameters which occur in the low-frequency range.

3.2. Design of compensators

Compensators are designed to overcome the dead zone and the time lag.

Since the size of the dead zone coming from the overlapped area of the spool valve is constant, we add the size of the dead zone to TDCSA input as follows:

$$\mathbf{u} = \mathbf{u}_{\text{tdcsa}} + \mathbf{u}_{\text{comp1}}, \tag{25}$$

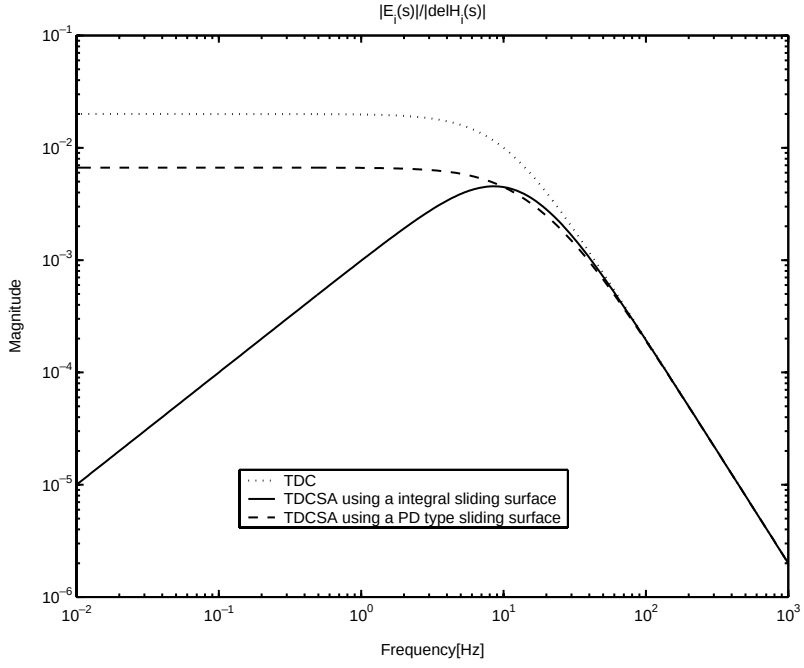

Fig. 6. Bode diagram of closed-loop error dynamics.

where $\mathbf{u}$ denotes the overall control input and $\mathbf{u}_{comp1}$ the 3×1 vector whose elements are constants equivalent to the dead zone of each link.

To compensate for the time lag, Chang and Lee (2002) designed the compensator using the pressure difference of the pump and cylinder. This compensator increases the pump pressure to cylinder pressure quickly and works until pump pressure begins to exceed the pressure of the cylinder plus the offset pressure, but it needs pressure sensors. In this paper, as shown in Fig. 7, we add the constant value ($\mathbf{u}_{comp2}$) to the control law until the pump pressure is increased to the pressure level sufficient to move the link, and then decrease the value slowly to zero once the link begins to move.

The whole control input, which now consists of the TDCSA input and the compensation inputs, is obtained as follows:

$$\mathbf{u} = \mathbf{u}_{tdcsa} + \mathbf{u}_{comp1} + \mathbf{u}_{comp2}. \quad (26)$$

Note that $\mathbf{u}_{comp2}$ is used for the control inputs of boom and arm.

4. Experiment

To evaluate TDCSA using an ISS in real circumstance, we have experimented the method in a heavy-duty excavator carrying out realistic tasks. The task of concern is primarily a straight-line motion in free spaces; yet, we have applied the straight-line motion to scraping the ground with the bucket in contact with the ground. The excavator used is a Hyundai Robex210LC-3, which has the following specifications: it weights 21 ton; the total length of the manipulator is 10.06 m and the total weight of boom, arm and bucket is 2.67 ton. In the experiments, the average speed of the bucket is set to be 0.5 m/s (4 m in 8 s), the speed level at which only an expert operator can perform a task.

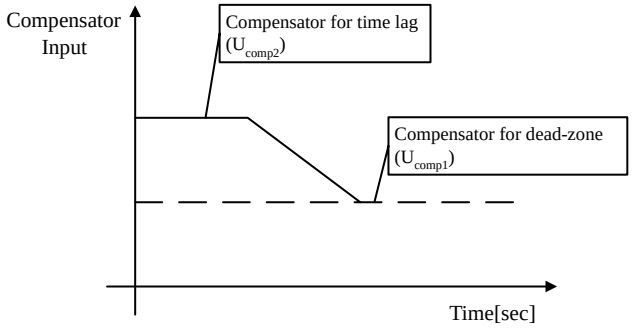

Fig. 7. Compensator for dead zone and time lag.

4.1. Experimental setup

Fig. 8 shows the overall structure of the excavator control system. The trajectories of boom, arm and bucket for a task are calculated on a DSP controller. The angles of each links are measured with a resolver and then converted by an A/D converter for generating a control input. The control input for each link is calculated on a DSP controller according to the control law, by using the trajectories generated and the angles measured. The control inputs obtained are converted through a D/A converter and fed to operate the electri-proportional pressure reducing (EPPR) valve, which transforms the electrical signal into the hydraulic pressure signal. The pilot pressure from the EPPR valve moves the spool of each main valve, thus making each link move. Here, the sampling frequency of a DSP controller is selected as 100 Hz.

4.2. Trajectory generation

To automate the straight-line motion, the trajectories of the end-effector and the joint angle are needed. Once the incline of the task surface is given, the end-effector path is determined, and then the velocity trajectory of the end-effector is determined by considering the average speed of the end-effector. Here, this velocity profile is for the direction tangential to the task surface, with the velocity in its normal direction being kept at 0 m/s. The displacement trajectory of the end-effector is obtained by integrating the velocity trajectory.

To control each link, the displacement trajectory of the end-effector is transformed into the joint angle trajectory of each link. Moreover, during a straight-line motion, the constraint exists that the attack angle of bucket (the angle of the bottom surface of bucket) is kept constant with respect to the task surface. The joint angles of boom and arm are calculated by

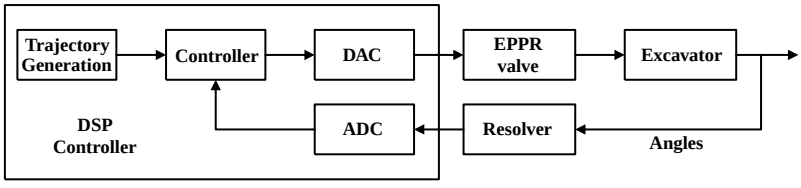

Fig. 8. Overall structure of control system.

using excavator kinematics from Fig. 9, as Eqs. (27) and (28):

$$\theta_{boom} = \sin^{-1}\frac{x_a^2 + y_a^2 + L_1^2 - L_2^2}{2L_1\sqrt{x_a^2 + y_a^2}} - \tan^{-1}\frac{y_a}{x_a}, \tag{27}$$

$$\theta_{arm} = \cos^{-1}\frac{x_a^2 + y_a^2 - L_1^2 - L_2^2}{2L_1L_2}, \tag{28}$$

where x_a and y_a is the position of the bucket joint. From the aforementioned constraint, the angle of the bucket is determined as follows:

$$\theta_{bucket} = \theta_{init} - \theta_{boom} - \theta_{arm}, \tag{29}$$

where θ_{init} is the sum of the boom angle, arm angle, and bucket angle in initial posture. From the above, we can determine the joint trajectory of each link.

We use the velocity trajectory obtained that meets the specified average speed of 0.5 m/s as shown in Fig. 10.

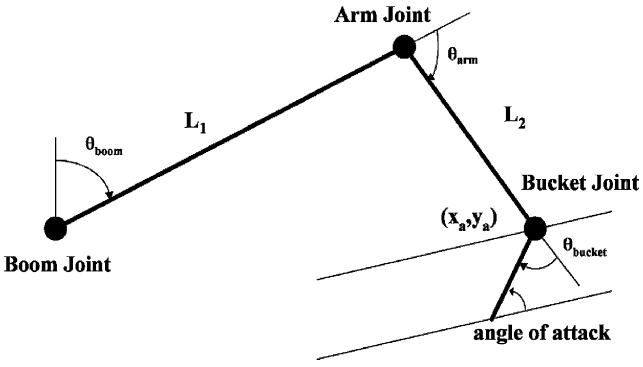

Fig. 9. Excavator kinematics.

Then, the joint trajectories for three task surfaces with respective inclines of -30°, 0° and 30° is shown in Fig. 11. This trajectory is made to realize the practice that straight-line motions are usually carried out from a stretched posture to a folded one.

4.3. Experimental results

In implementing the control law in Eq. (15), we determined each gain for $\mathbf{u}_{\text{tdcsa}}$ as follows:

$$\bar{\mathbf{M}} = \begin{bmatrix} \bar{M}_1 & 0 & 0 \\ 0 & \bar{M}_2 & 0 \\ 0 & 0 & \bar{M}_3 \end{bmatrix},$$

$$\mathbf{K}_v = \begin{bmatrix} 2\xi_1 w_1 & 0 & 0 \\ 0 & 2\xi_2 w_2 & 0 \\ 0 & 0 & 2\xi_3 w_3 \end{bmatrix},$$

$$\mathbf{K}_p = \begin{bmatrix} w_1^2 & 0 & 0 \\ 0 & w_2^2 & 0 \\ 0 & 0 & w_3^2 \end{bmatrix}, \tag{30}$$

where ξ_i and w_i denote the damping coefficient and the frequency for desired error dynamics of each link. In addition, $\bar{M}_i$ is selected in the stable range through experiments. The switching gain (K_{w_i}), satisfying the condition of $(K_w)_{ii} > |(\Delta H)_i|$, is selected by tuning. The boundary layer of the saturation function (ϕ_i) is

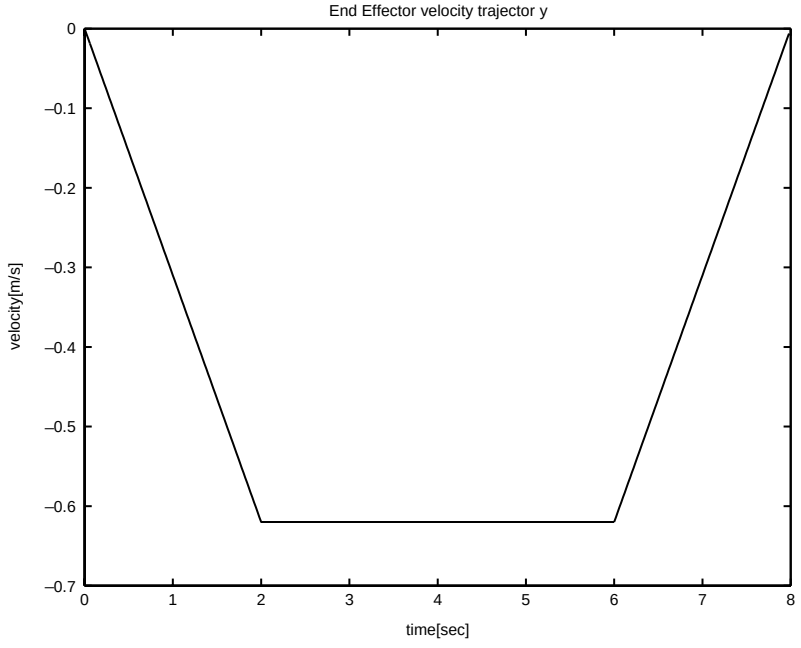

Fig. 10. End-effector's velocity trajectory for horizontal direction.

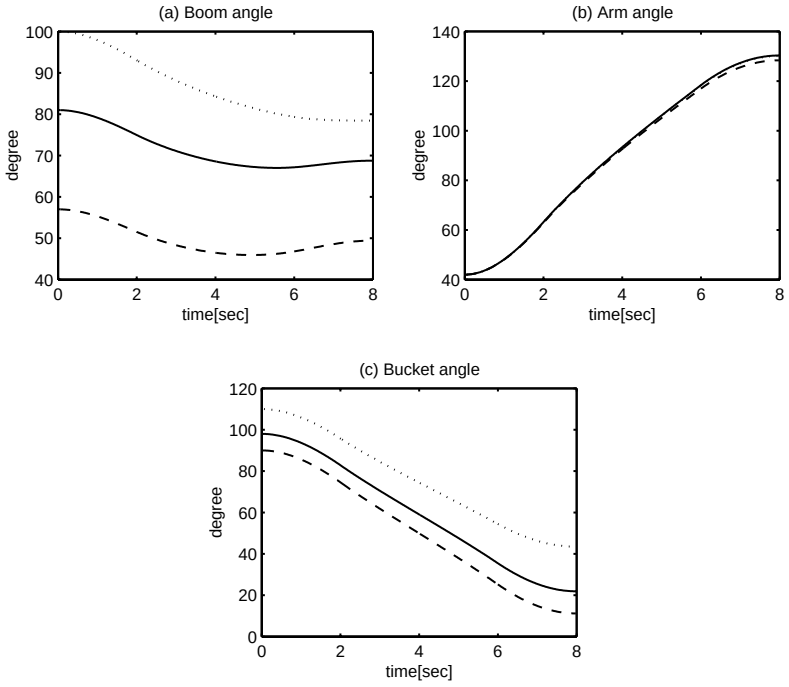

Fig. 11. Angle trajectories for task surface (solid line stands for incline of 0°; dashed line for incline of 30°; and dotted line for incline of −30°).

properly chosen by tuning, without the chattering. Then, the magnitude of $\mathbf{u}_{comp2}$ is to be tuned from a small value until satisfactory performance is achieved.

4.3.1. Noncontact condition

In free spaces, we experimented with three controllers: TDC, TDCSA using a PDSS and TDCSA using an ISS; for task surfaces with inclines of $-30°$, $0°$ and $30°$, respectively. Here, among the gains of the TDCSA, the desired error dynamics are the identical with those of TDC. The switching gain of the TDCSA using an ISS is identical with that of the TDCSA using a PDSS.

Fig. 12 shows the experimental results for TDC. As shown in Fig. 12, the vertical distance error of the end-effector is within ± 3 cm for the task surface with an incline of $-30°$. For the task surface with an incline of $30°$, however, the vertical distance error is within ± 6 cm. According to the task surface and joint positions, the tracking error of the boom varies greatly. Namely, the control performance for the TDC varies greatly with the task surface and joint positions.

The experimental results for the TDCSA using a PDSS and for the TDCSA using an ISS are shown in Figs. 13 and 14, respectively. The control performance of TDCSA is better than that of TDC. The control performance of TDCSA does not vary greatly with the task surface and joint positions. The whole vertical distance error of the end-effector is within ± 4 cm for TDCSA using an ISS, whereas the vertical distance error is over ± 4 cm for TDCSA using a PDSS.

Fig. 15 shows the experimental results of the above three controllers for the task surface with an incline of $0°$, and Fig. 16 shows the power spectral density of the tracking errors in Fig. 15. In Fig. 15, the difference due to TDCSA using an ISS is not that significant; yet there exists a noticeable trend. As shown in Fig. 16, TDCSA using an ISS results in the DC components of the power spectral densities considerably smaller than those of the other two controllers. This trend is a direct outcome of the offset of the tracking error of TDCSA using an ISS smaller than those of the other two controllers. A close inspection of the tracking errors in Fig. 15 (a) reveals that the tracking error due to TDCSA using an ISS tends to fluctuate *around zero*, whereas those due to the other controllers tend to *drift from zero*. These results suggest that TDCSA using an ISS can decrease the offset of the tracking error effectively, which still occurs for TDC and TDCSA using a PDSS.

4.3.2. Contact condition

The above experiments do not involve any contact with the ground; but the straight-line motion in free spaces. Therefore digging or excavating work is not our immediate concern. Nevertheless, we have applied the straight-line motion to leveling work, scraping the ground with the bucket in contact with the ground. When leveling work is being done, friction due to the contact behaves as a disturbance to position control of TDCSA using an ISS. Since TDCSA using an ISS has

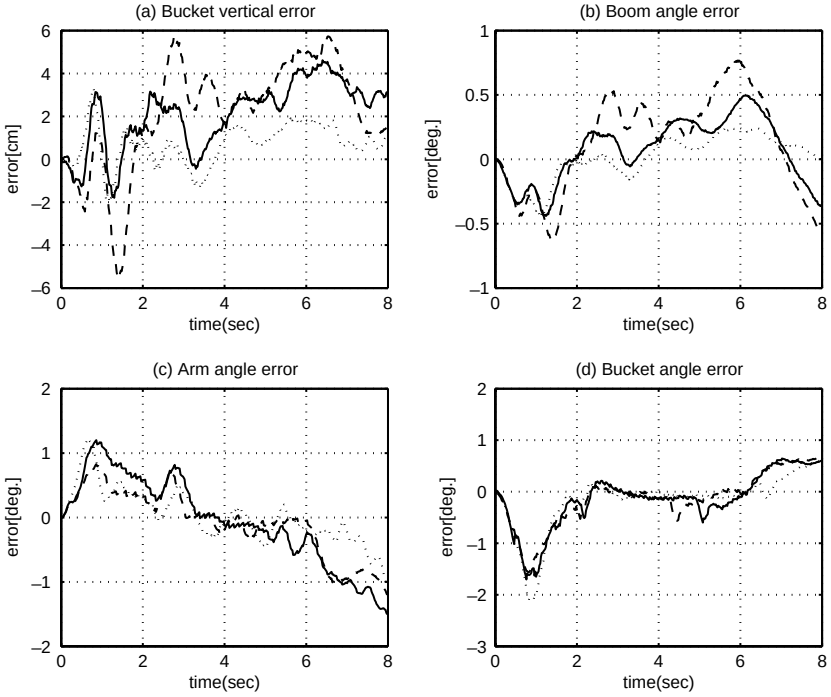

Fig. 12. Experimental results of TDC for task surface (solid line stands for incline of 0°; dashed line for incline of 30°; and dotted line for incline of −30°).

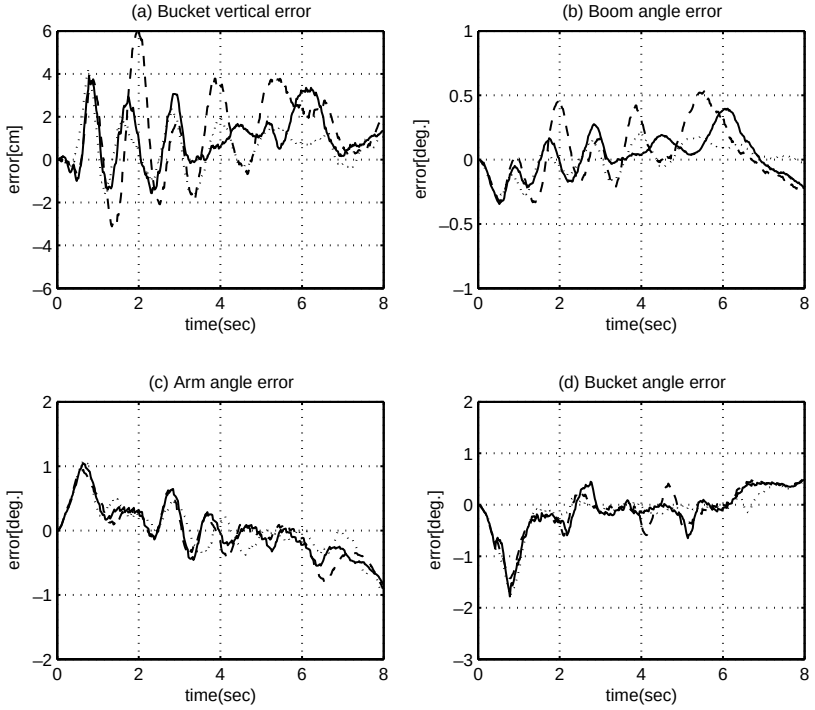

Fig. 13. Experimental results of TDCSA using a PDSS for task surface (solid line stands for incline of 0°; dashed line for incline of 30°; and dotted line for incline of −30°).

shown effectiveness in rejecting the disturbances, it does not require additional force control scheme.

We have applied TDCSA using an ISS to leveling works for the ground surfaces with inclines of −30°, 0° and 30°, respectively. The soil used at the experiments is classified into gravel (GP group)—poorly graded gravel and graded-sand mixtures—by the United Soil Classification, a generally used classification in civil

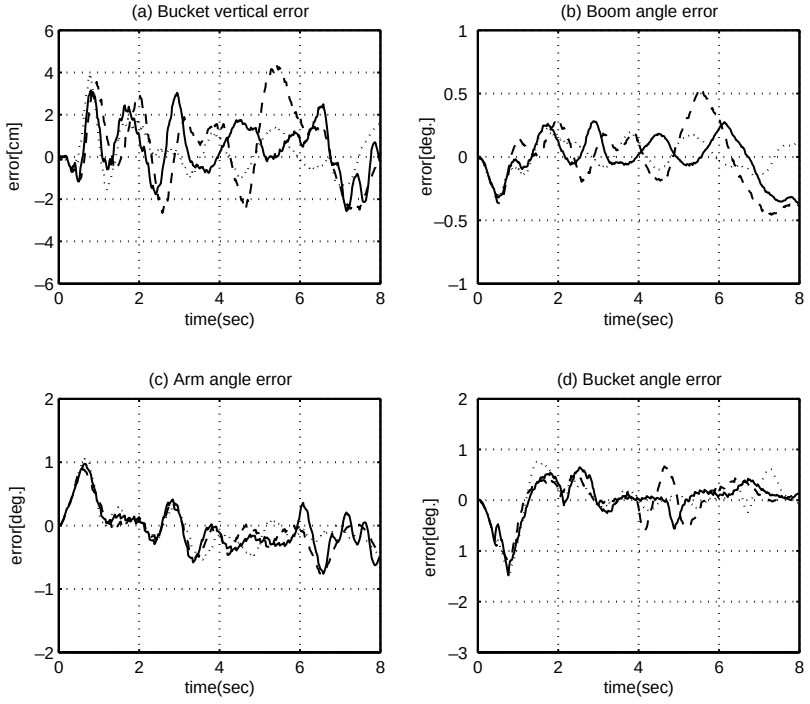

Fig. 14. Experimental results of TDCSA using an ISS for task surface (solid line stands for incline of 0°; dashed line for incline of 30°; and dotted line for incline of −30°).

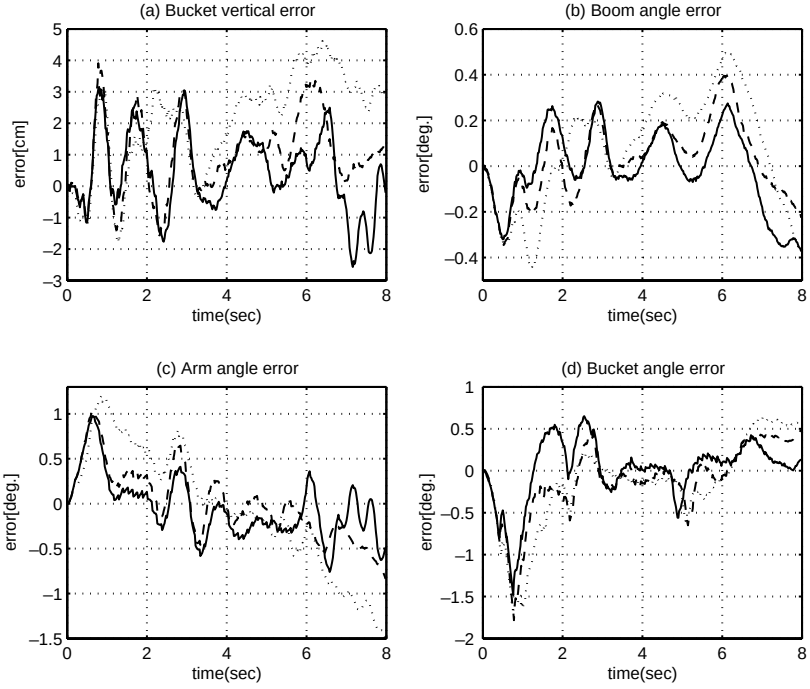

Fig. 15. Experimental results for task surface with incline of 0° (solid line stands for TDCSA using an ISS; dashed line for TDCSA using a PDSS; and dotted line for TDC).

engineering (Bowles, 1982). Fig. 17 (a) shows the experimental results that the bucket vertical error is mostly within ±4 cm for three task surfaces, which is similar to the results for non-contact condition. On the contacting condition, the ground will prevent the bucket vertical error from having the large error of (-) direction by supporting the end-effector of the excavator, and the friction force between the end-effector and the ground

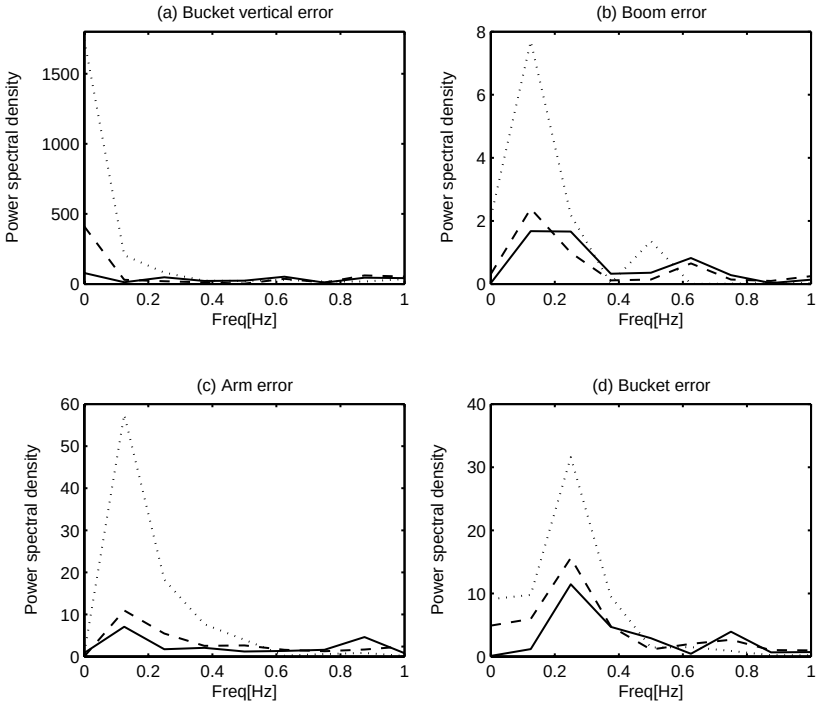

Fig. 16. Power spectral density of tracking errors for task surface with incline of 0° (solid line stands for TDCSA using an ISS; dashed line for TDCSA using a PDSS; and dotted line for TDC).

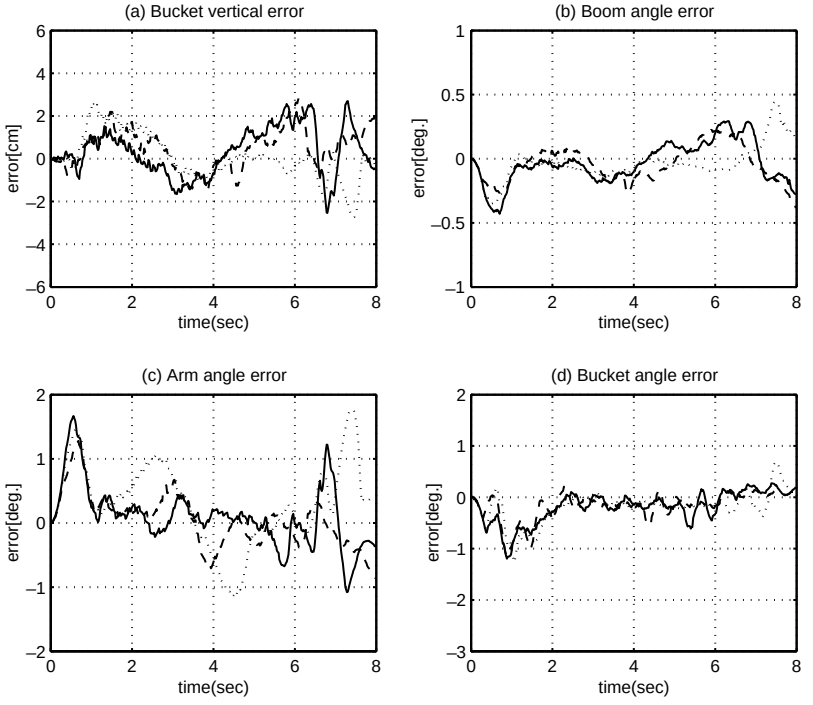

Fig. 17. Experimental results for TDCSA using an ISS for task surface in contact the end-effector with the ground (solid line stands for incline of 0°; dashed line for incline of 30°; and dotted line for incline of −30°).

deteriorates the control performance of the arm link; however, it does not affect largely the error of the bucket vertical error due to the posture of the excavator. These results verify that the position control approach based on the TDCSA is effective in handling the contact condition.

From the experimental results of applying TDCSA using an ISS to a 21-ton robotic excavator, the vertical

distance error of the end-effector is mostly within ± 4 cm for the task surfaces with inclines of $0, -30^\circ$ and 30°, respectively. Considering that the accuracy achieved by an expert operator is usually within an error of ± 5 cm at 0.5 m/s speed level, these results verify good tracking performance of our proposed control law.

5. Conclusion

A TDCSA using an ISS was proposed in this paper for the control of a 21-ton robotic excavator. From analysis, we observed that the proposed control is more robust against the disturbances and the parameter variations, which occur in the low-frequency range, than that of TDC and TDCSA using a PDSS. Through experiments, we observed that TDCSA using an ISS is effective enough to control a 21-ton robotic excavator; and that our proposed control achieves better tracking performances than an expert operator does. Considering that the experiments have been made over a broad motion range, under realistic working speed conditions, and on task surfaces with various inclines, we can confirm the validity of our proposed control algorithm.

Appendix A. Dynamic modeling of the excavator system

We will obtain the brief model of the robotic excavator to design the controller. More details about the model of a robotic excavator can be found in Chang and Lee (2002).

The dynamics of the manipulator consisting of boom, arm and bucket can be mathematically modeled as follows:

$$\mathbf{F} = \mathbf{M}_l(\mathbf{l})\ddot{\mathbf{l}} + \mathbf{V}_l(\mathbf{l}, \dot{\mathbf{l}}) + \mathbf{G}_l(\mathbf{l}) + \mathbf{Fr}_l(\mathbf{l}, \dot{\mathbf{l}}), \tag{A.1}$$

where $\mathbf{F}$ denotes the 3×1 vector of forces acting on the pistons in the cylinders, and $\mathbf{l}$ is the 3×1 vector, each element of which represents the piston displacement relative to the cylinder responsible for each link. $\mathbf{M}_l(\mathbf{l})$ is the 3×3 inertial matrix, $\mathbf{V}_l(\mathbf{l}, \dot{\mathbf{l}})$ is the 3×1 vector of centrifugal and Coriolis terms, $\mathbf{G}_l(\mathbf{l})$ is the 3×1 vector of gravity terms, and $\mathbf{Fr}_l(\mathbf{l}, \dot{\mathbf{l}})$ is the 3×1 vector consisting of various friction terms.

Fig. 18 shows the hydraulic actuator circuit of a Hyundai Robex210LC-3. In Fig. 18, the flow from pump 1 is divided and supplied to the boom cylinder and the bucket cylinder, via main valves; whereas pump 2 supplies flow to the arm cylinder. Fig. 19 shows one set of a main valve and cylinder pertaining to a specific link.

Now, consider the divide above, ignoring the compressibility of oil at junctions (a)–(c) in Fig. 19. Then, from the continuity equation of flow at junctions (a)–(c) and a linearized valve flow equation (Chang & Lee, 2002), one can obtain linearized relationships of at each

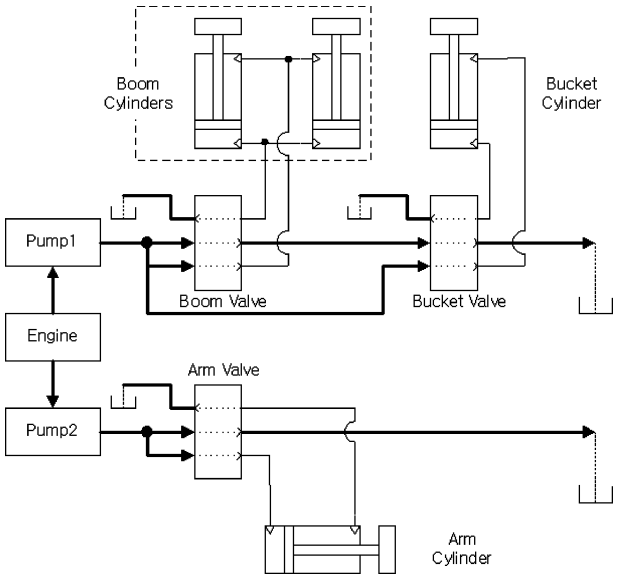

Fig. 18. Overall structure of the hydraulic circuit for boom, arm and bucket.

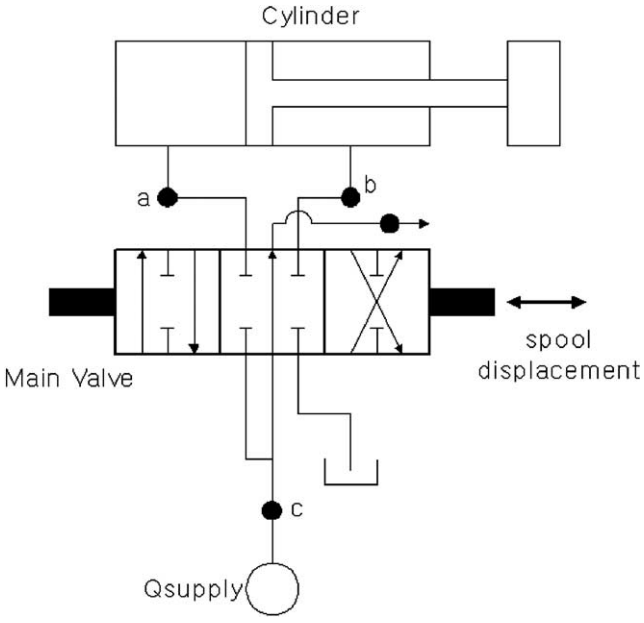

Fig. 19. Detailed structure of the hydraulic circuit pertaining to a link (boom, arm and bucket).

link as follows:

$$\begin{bmatrix} K_{pa\_ai} & 0 & K_{pa\_ci} \\ 0 & K_{pb\_bi} & K_{pb\_ci} \\ K_{pc\_ai} & K_{pc\_bi} & K_{pc\_ci} \end{bmatrix} \begin{bmatrix} P_{ai} \\ P_{bi} \\ P_{ci} \end{bmatrix}$$

$$= \begin{bmatrix} A_{ai}\dot{l}_i - K_{u\_ai}u_i - Q_{rm\_ai} \\ A_{bi}\dot{l}_i - K_{u\_bi}u_i - Q_{rm\_bi} \\ Q_{\mathrm{sec}\_i} - K_{u\_ci}u_i - K_{pc\_di}P_{di} - Q_{rm\_ai} \end{bmatrix}, \tag{A.2}$$

where $i = 1, 2, 3$ denote subscripts representing boom, arm and bucket, respectively; A_{ai} and A_{bi} the areas of two sides of the piston in the cylinder; Q_{sec_i} the flow from the pump mainly for ith cylinder; u_i the displacement of each spool, which is the input to the system; $K_{p(.)}$ and $K_{u\_(.)}$ denotes valve flow gain and valve flow-pressure coefficient; P_{ai}, P_{bi}, P_{ci}, and P_{di} denote pressures at junctions (a)–(d), respectively. In addition, Q_{rm_ai}, Q_{rm_bi} and Q_{rm_ci} stand for higher-order terms in the Taylor series expansion.

From the force balance of a piston in the cylinders, we have

$$F_i = A_{ai}P_{ai} - A_{bi}P_{bi}, \tag{A.3}$$

where F_i denotes ith element of force vector, F, in Eq. (A.1). Solving for P_{ai} and P_{bi} from Eq. (A.2) and substituting them into Eq. (A.3), one obtains the following relationship between the input u_i and the force F_i:

$$F_i = K_{u\_i}u_i + K_{l\_i}\dot{l}_i + Q_{etc\_i}, \tag{A.4}$$

where K_{u_i} and K_{l_i} denote the coefficients of u_i and $\dot{l}_i$, respectively; and Q_{etc_i} represents all the terms that do not include either u_i or $\dot{l}_i$.

Combining Eq. (A.1) with Eq. (A.4), the whole model is obtained as follows:

$$\mathbf{u} = \mathbf{M}_K\ddot{\mathbf{l}} + \mathbf{H}, \tag{A.5}$$

where

$$\mathbf{M}_K = diag(K_{u\_1}^{-1}, K_{u\_2}^{-1}, K_{u\_3}^{-1})\mathbf{M}_l,$$

$$\mathbf{H} = [h_1 \quad h_2 \quad h_3], \quad \text{with}$$

$$h_i = K_{u\_i}^{-1}(v_i + g_i + fr_i - K_{l\_i}\dot{l}_i - Q_{etc\_i})$$

with $diag(\cdot)$ denoting a diagonal matrix, v_i, g_i and fr_i being ith element of $\mathbf{V}_l, \mathbf{G}_l$ and $\mathbf{Fr}_l$ in Eq. (A.1), respectively.

References

Bowles, J. E. (1982). *Foundation analysis and design*, New York: McGraw-Hill, pp. 26–27.

Bradley, D. A., & Seward, D. W. (1998). The development, control and operation of an autonomous robotic excavator. *Journal of Intelligent and Robotic Systems*, *21*, 73–97.

Chang, P. H., & Lee, S. J. (2002). A straight-line motion tracking control of hydraulic excavator system. *Mechatronics*, *12*(1), 119–138.

Chang, P. H., & Park, S. H. (1998). The development of anti-windup scheme and stick-slip compensator for time delay control. *Proceedings of the American control conference* (pp. 3629–3633).

Chiba, J., & Takeda, T. (1982). Automatic control in civil engineering construction machinery. *Journal of the Society of Instrument and Control Engineers*, *21*(8), 800–806.

Hsia, T. C., & Gao, L. S. (1990). Robot manipulator control using descentralized linear time-invariant time-delayed joint controllers. *Proceedings of IEEE conference on robotics and automation* (pp. 2070–2075).

Lee, C. C. (1993). *A study on the design of fuzzy logic controller for bucket tip leveling of hydraulic excavator*. Ph.D. thesis, Seoul National University.

Lee, J. H., & Youn, M. J. (1999). A new integral variable structure regulation controller for robot manipulators with accurately predetermined output. *ISIE'99. Proceedings of the IEEE international symposium on industrial electronics* (pp. 336–341).

Medanic, J., Yuan, M., & Medanic, B. (1997). Robust multivariable nonlinear control of a two link excavator: Part I. *Proceedings of the IEEE conference on decision and control* (pp. 4231–4236).

Morita, T., & Sakawa, Y. (1986). Modeling and control of a power shovel. *Proceedings of the Japan society of measurement and automatic control* (Vol. 22(1)) (pp. 68–75).

Sepehri, N., Lawrence, P. D., Sassani, F., & Frenette, R. (1994). Rosolved-mode teleoperated control of heavy-duty hydraulic machines. *ASME Journal of Dynamic System, Measurement and Control*, *116*(2), 232–240.

Singh, S. (1997). State of art in automation of earthmoving. *ASCE Journal of Aerospace Engineering*, *10*(4), 179–188.

Slotine, J.-J. E., & Li, W. (1991). *Applied nonlinear control* (pp. 276–309). Englewood Cliffs, NJ: Prentice-Hall.

Song, B., & Koivo, A. J. (1995). Neural adaptive control of excavators. *Proceedings of the IEEE/RSJ conference on intelligent robots and systems* (pp. 162–167).

Stentz, A., Bares, J., Singh, S., & Rowe, P. (1998). A robotic excavator for autonomous truck loading. *IEEE International conference on intelligent robot and systems* (pp. 1885–1893).

Utkin, V., & Shi, J. (1996). Integral sliding mode in systems operating under uncertainty conditions. *Proceedings of the IEEE conference on decision and control* (pp. 4591–4596).

Yokota, S., Sasao, M., & Ichiryu, K. (1996). Trajectory control of the boom and arm system of hydraulic excavators. *Transactions of the Japan Society of Mechanical Engineers Part C*, *62*(593), 161–167.

Youcef-Toumi, K., & Ito, O. (1990). A time delay controller for systems with unknown dynamics. *ASME Journal of Dynamic System, Measurement and Control*, *112*, 133–141.